scientific reports

Check for updates

OPEN

Yolk–shell structured magnetic mesoporous silica: a novel and highly efficient adsorbent for removal of methylene blue

Reza Mirbagheri, Dawood Elhamifar✉ & Masoumeh Shaker

In this study, a novel magnetic mesoporous silica with yolk–shell structure (Fe_3O_4@Void@m.SiO_2) was successfully synthesized via a polymer-template assisted method. The Fe_3O_4@Void@m.SiO_2 was characterized by using FT-IR, EDS, SEM, TEM, VSM, PXRD and nitrogen adsorption–desorption analyses. The Fe_3O_4@Void@m.SiO_2 nanocomposite showed high efficiency in adsorption of an organic dye and water pollutant called methylene blue (MB) with 98.2% removal capability. Furthermore, the effect of different parameters in the adsorption of MB was investigated. Different models of kinetic were examined and compared with each other. The recoverability and reusability of designed Fe_3O_4@Void@m.SiO_2 material were also studied under applied conditions.

After the first report about interesting materials with yolk–shell (YS) structure[1], many researches have developed the synthesis methods and properties of these materials with different names such as nanorattle[2], movable core/shell[1], core/shell with hollow interiors[3] and yolk/shell[4]. These nanomaterials are in the center of attention due to interesting properties such as high surface area, interstitial hollow space and low density[5,6]. These special properties make yolk–shell nanocomposites suitable to use in the fields of biomedical[7], lithium batteries[8,9], sensors[10,11], catalysis[12–16] and adsorption[17,18]. Some of recently reported yolk–shell structured materials are Sn_4P_3@C[19], Sn@SnO/SnO_2[20], Al@TiO_2 NPs[21] and Au-CeO_2@ZrO_2[22]. Among different shells, silica-based ones is more important in catalysis and adsorption processes owing to its high loading capacity compared to other shells[23,24]. The preparation methods effect on features of the yolk, space, thickness, porosity and shape of YS materials. The more common methods used for the preparation of YSs are hard temple-assisted, soft template-assisted and template-free[25]. Among these, the soft template method has attracted more attention due to easy removal of template and also economically friendly[26,27].

Moreover, owing to superparamagnetic properties, easy separation and low toxicity, magnetic nanoparticles (MNPs) have been so interested in different fields such as biomedical[28,29], magnetic resonance imaging[30], drug delivery[31] and separation[32]. However, the most of MNPs suffer from disadvantages of aggregation, biodegradation and low capacity. In order to increase the stability and capacity, these NPs are composited with different species. Among different species, mesoporous silica is more attracted because of its high surface area, high pore volume and high capacity[33–35].

As regards to water purification importance and lots of different pollutants that made by pharmaceutical, paper making, textile, leather, etc., different methods such as photocatalytic degradation, adsorption and oxidation have been used to eliminate water pollutants[36,37]. To date many adsorbents have been applied for the elimination of organic and inorganic pollutants from water. Among these, magnetic NPs have attracted more attention due to the advantages of easy magnetically separation, economically friendly and high efficiency. Some of recently developed systems are magnetic zeolites[38], magnetic carbon nanotubes composites[39], Zn/ferrite/graphene oxide[40] and activated carbon/$NiFe_2O_4$[41]. Although these adsorbents gave good to high efficiency in the removal of water pollutants, however, in spite of high adsorption capacity of the yolk–shell based magnetic nanocomposites, according to our knowledge, there is no report in the study of efficiency of these type nanomaterials in the removal of water pollutants. In view of the above, herein, a novel magnetic Fe_3O_4@mesoporous silica nanocomposite (Fe_3O_4@Void@m.SiO_2) with yolk–shell structure and high magnetic properties is prepared for adsorption of methylene blue (MB) from water. The kinetics, isotherm and equilibrium data for adsorption of MB have been analyzed and different models have been employed to understand the mechanism.

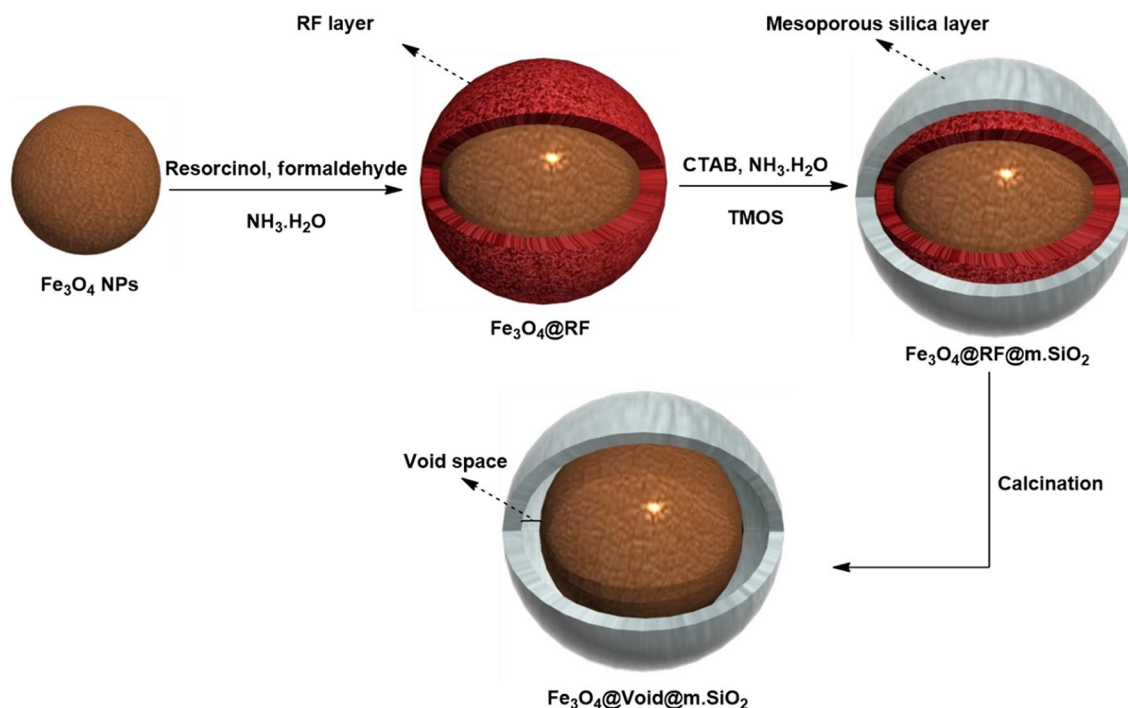Department of Chemistry, Yasouj University, 75918-74831 Yasouj, Iran. ✉email: d.elhamifar@yu.ac.ir

nature portfolio

1

Figure 1. Preparation of Fe_3O_4@Void@m.SiO_2.

Experimental section

Preparation of Fe_3O_4@Void@m.SiO_2 nanomaterial. To do this, firstly magnetic Fe_3O_4 NPs were prepared[42]. In the second step, the Fe_3O_4 NPs were modified with resorcinol–formaldehyde polymer to form Fe_3O_4@RF material. In order to prepare Fe_3O_4@RF, the Fe_3O_4 NPs (100 mg) were added to a mixture of EtOH (20 mL) and H_2O (10 mL) in an ultrasonic bath. Then, ammonium hydroxide (0.5 g, aqueous solution, 28 wt %), HCHO (0.1 g, 37 wt %) and resorcinol (0.1 g, 0.09 mM) were added while stirring for 2 h. After polymerization, the resulted Fe_3O_4@RF was collected and washed completely with H_2O and EtOH. Next, the as-made Fe_3O_4@RF (0.12 mg) was dispersed in a mixture of CTAB (0.45 g), ammonia (2 mL, 28 wt %), H_2O (100 mL) and EtOH (150 mL). The resulted combination was stirred to form a homogeneous mixture. After adding of TMOS (1.5 mL), stirring was continued for 6 h. The resulted Fe_3O_4@RF@m.SiO_2 material was washed completely with EtOH and H_2O. Finally, the RF layer and CTAB surfactant were removed after heating of the Fe_3O_4@RF@m. SiO_2 material at 550 °C for 6 h (Fig. 1). The final magnetic nanomaterial with yolk–shell structure was denoted as Fe_3O_4@Void@m.SiO_2.

Adsorption process. For this, 5 mg of the Fe_3O_4@Void@m.SiO_2 was added in 15 mL of an aqueous solution of MB. This mixture was shaken continuously and the Fe_3O_4@Void@m.SiO_2 was magnetically separated immediately. The MB concentration was measured by UV–vis at 665 nm. The adsorption efficiency for MB in water solution was calculated by using Eq. (1).

$$\text{adsorption efficiency (\%)} = \frac{C_0 - C_e}{C_0} \times 100 \tag{1}$$

On the other hand, the amount of adsorbed MB on the adsorbent (q_e) was calculated by using Eq. (2).

$$q_e = \frac{(C_0 - C_e) \times V}{m} \tag{2}$$

Herein, C_0 and C_e are, respectively, the concentration of the initial dye solution and the residual dye solution that quantitatively estimated by linear regression equations resulted at different dye concentrations, V is solution volume in liters and m is adsorbent amount (mg).

Results and discussion

The magnetic mesoporous silica material (Fe_3O_4@Void@m.SiO_2) with yolk–shell structure was prepared from an intermediate structure (Fe_3O_4@RF) which was made by polymerization of HCHO and resorcinol (Fig. 2) on the Fe_3O_4NPs surface. The mesoporous silica shell was coated on the Fe_3O_4@RF by using CTAB and TMOS via a sol–gel approach. Finally, RF and CTAB were eliminated to deliver Fe_3O_4@Void@m.SiO_2 (Fig. 1).
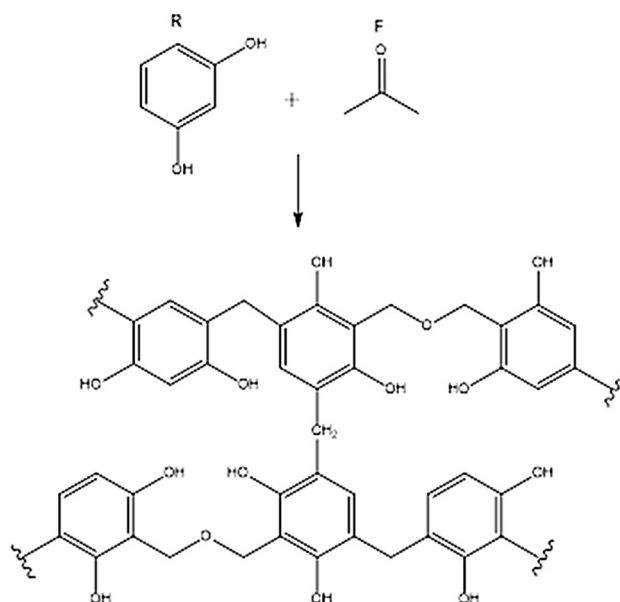
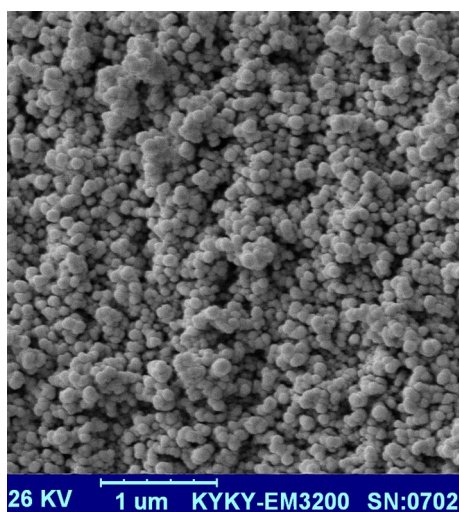**Figure 2.** A suitable pathway for polymerization of formaldehyde and resorcinol.

Figure 3. SEM image of the Fe_3O_4@Void@m.SiO$_2$ nanomaterial.

Characterization. The SEM image of Fe_3O_4@Void@m.SiO$_2$ yolk shell nanomaterial is illustrated in Fig. 3. As shown, the designed material has particles with spherical morphology and average size of 84 nm. These types of NPs are excellent candidates for adsorption processes.

The TEM image of the Fe_3O_4@Void@m.SiO$_2$ nanomaterial also showed a yolk–shell structure with black cores (Fe_3O_4 NPs) and mesoporous silica shell (Fig. 4).

The low-angle PXRD (LA-PXRD) pattern of Fe_3O_4@Void@m.SiO$_2$ showed an intense peak centered at 2 theta of 1 degree that is characteristic of nanomaterials with an ordered 2D hexagonal mesostructure (Fig. 5). These types of materials have high surface area and are very effective in the adsorption processes.

The wide-angle PXRD of Fe_3O_4@Void@m.SiO$_2$ showed six reflection peaks at 2θ of 63°, 57°, 54°, 43°, 35° and 30° (Fig. 6). This pattern is in good agreement with the PXRD pattern of Fe_3O_4 NPs confirming high stability of the magnetite cores during material preparation. This analysis also showed a broad peak at 2 theta about 20 degree that is attributed to mesoporous silica shell[42].

Figure 7 shows the vibrating sample magnetometer (VSM) analysis of the designed nanomaterial. As shown, this material has good magnetic property. As expected, due to the nonmagnetic mesoporous silica shell and the large void space, the magnetization is reduced from 60 for Fe_3O_4 to 15 emu/g for Fe_3O_4@Void@m.SiO$_2$[14].

The FT-IR spectra of Fe_3O_4 and Fe_3O_4@Void@m.SiO$_2$ before and after calcination, are shown in Fig. 8. For all materials, the absorption peaks of Fe–O bonds are observed about 580 cm^{-1}. The bands at 710–810 cm^{-1} are
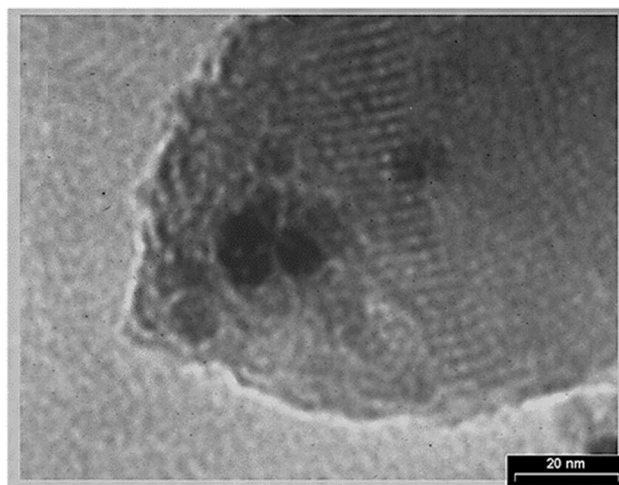
Figure 4. TEM image of Fe_3O_4@Void@m.SiO_2.
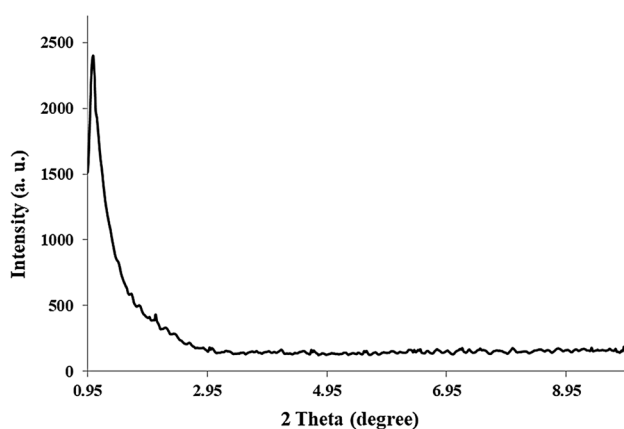
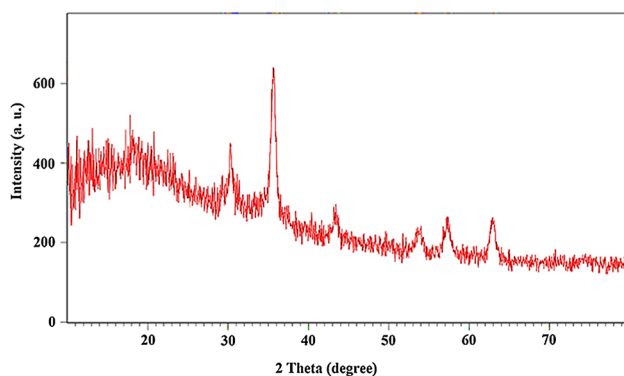**Figure 5.** The low angle PXRD pattern of Fe_3O_4@Void@m.SiO_2.

Figure 6. The wide-angle PXRD pattern of Fe_3O_4@Void@m.SiO_2.

due to C–Si. The peaks cleared at 1100 and 935 cm^{-1} are due to Si–O–Si bonds. The peak at 3500 cm^{-1} is owing to O–H bonds of material surface. Before surfactant and RF removal, the peaks at 2850 and 2920 cm^{-1} are corresponded to aliphatic C–H bonds of CTAB and peaks about 3020 cm^{-1} are related to aromatic C–Hs of RF (Fig. 8B). Interestingly, the latter peaks are disappeared in Fig. 8C confirming successful removal of CTAB and RF during calcination. It is important to note that, to prepare a material with mesoporous yolk–shell structure, both CTAB (containing aliphatic C–H) and RF (containing aromatic C–H) should be romed. After removal of CTAB a mesoporous silica shell is resulted, while after removal of RF the void space between shell and core is resulted.
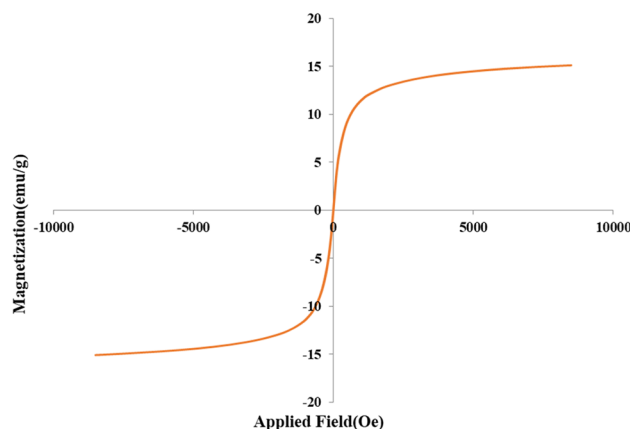
Figure 7. The VSM analysis of Fe_3O_4@Void@m.SiO$_2$.

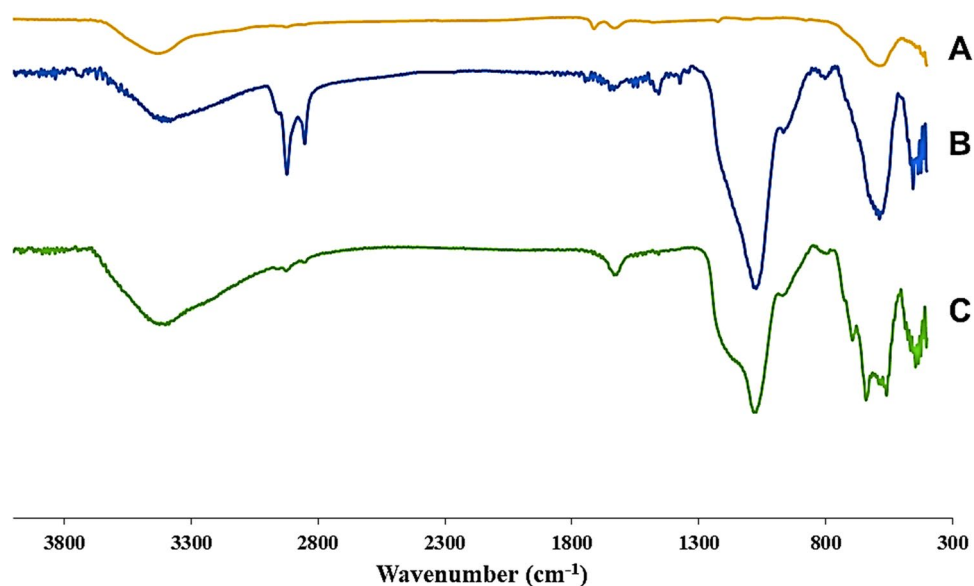**Figure 8.** FT-IR results of Fe_3O_4 (**A**), Fe_3O_4@Void@m.SiO$_2$ nanomaterial before (**B**) and after (**C**) calcination.

The EDS was performed for elemental analysis of the material before adsorption process (Fig. 9). This analysis clearly showed the existence of oxygen, iron and silicon confirming high stability and well incorporation of expected magnetite cores and silica shells in the material network.

The nitrogen adsorption–desorption isotherm of the Fe_3O_4@Void@m.SiO$_2$ nanomaterial before adsorption process shows a type IV isotherm with an H2 hysteresis loop, which is characteristic of ordered mesostructures with high regularity (Fig. 10). The sharp capillary condensation steps occurred at a relative pressure of 0.45–0.97, indicate the large void space of Fe_3O_4@Void@m.SiO$_2$ and the porous silica shell[43]. The Brunauer–Emmett–Teller (BET) surface area and total pore volume of the material were also found to be 666.16 m^2/g and 1.28 cm^3/g, respectively. The Barrett–Joyner–Halenda (BJH) pore size distribution isotherm showed a bimodal size distribution at 7.1 and 12.2 nm related to the mesoporous shell and void space between yolk and shell, respectively (Fig. 11). These data are in good agreement with LA-PXRD and TEM results confirming the presence of a mesoporous shell and yolk–shell structure for the designed nanomaterial.

Adsorption Studies. The elimination of MB, as organic dye, was examined as a model to study adsorption ability of synthesized Fe_3O_4@Void@m.SiO$_2$ material. The time, dye concentration, amount of adsorbent and adsorption pH were optimized as well as different models were checked in kinetic and isotherm studies.

Effect of pH. The effect of pH was investigated due to the structure and ionization degree of the MB dye can be influenced by pH value[44]. The pKa of MB is 3.8[45], therefore, at pH values above this, the preponderant MBs are cationic. The effect of pH values was studied during 5 min using 0.005 g of the adsorbent (Fig. 12). At acidic pH, the –OHs of mesoporous silica shell and magnetic core interact with MBs via H-bonding. At basic pH, Si–
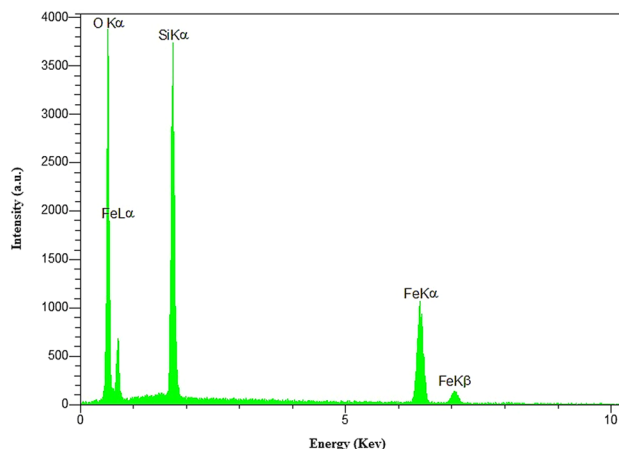
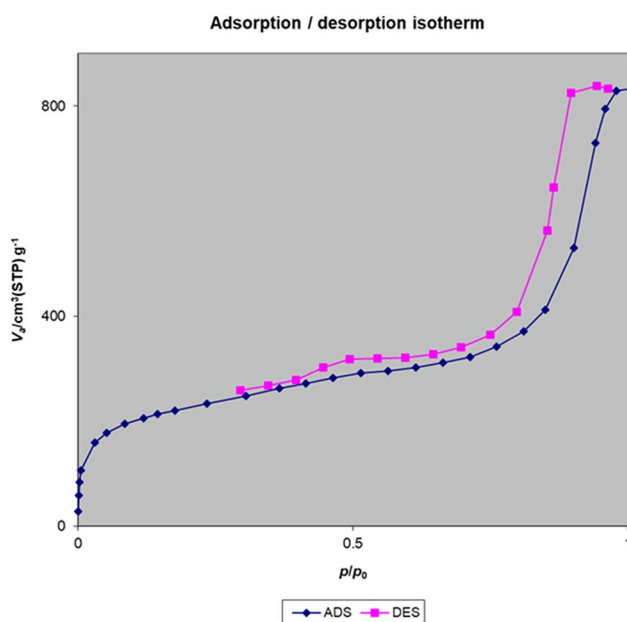**Figure 9.** EDS analysis of Fe$_3$O$_4$@Void@m.SiO$_2$ nanomaterial before adsorption process.

Figure 10. Nitrogen adsorption–desorption isotherm of the Fe$_3$O$_4$@Void@m.SiO$_2$ nanomaterial before adsorption process.

O− and Fe–O− are the greater groups due to the deprotonation of Si–OH and Fe–OH, respectively. These sites improve the electrostatic interaction between the cationic dye and the anionic charged surfaces (Fig. 13). Similar results have been reported for MB elimination using clay[46,47] and activated coal[48]. Another important factor for this adsorption process is H-bonding interactions between N-sites of dye and OH sites of adsorbent. It is important to note that the aforementioned interactions can occur on both inner and outer surfaces of mesoporous silica shell and also on outer surface of magnetite cores[49,50]. According these findings, a suitable mechanism for this adsorption process is proposed in Fig. 13. According to this experiment, at pH 9.0 the best result was obtained. Therefore, this was used as optimum pH in the subsequent tests.

Effect of adsorbent dosage and dye concentration.   In next step, the amounts of adsorbent and dye concentration were optimized (respectively, Figs. 14 and 15). It is clear that the adsorbent amount and the numbers of active positions on its surface affect the adsorption rate. By increasing the amount of adsorbent, the vacant and unoccupied positions are increased and thus the percentage of removal is increased. While, after this, there is a little change in the adsorption process. As shown in Fig. 14, the optimum amount of adsorbent is 0.005 g for 15 mL of MB aqueous solution (5 ppm) with 98.2% removal. This confirms high performance of the designed material in the MB removal. In the next, the effect of dye concentration using a constant amount (0.005 g) of adsorbent was studied. As shown in Fig. 15, by increasing the amount of MB concentration, the removal performance of a certain amount of Fe$_3$O$_4$@Void@m.SiO$_2$ is reduced which it refers to disproportionate in amount of active sites
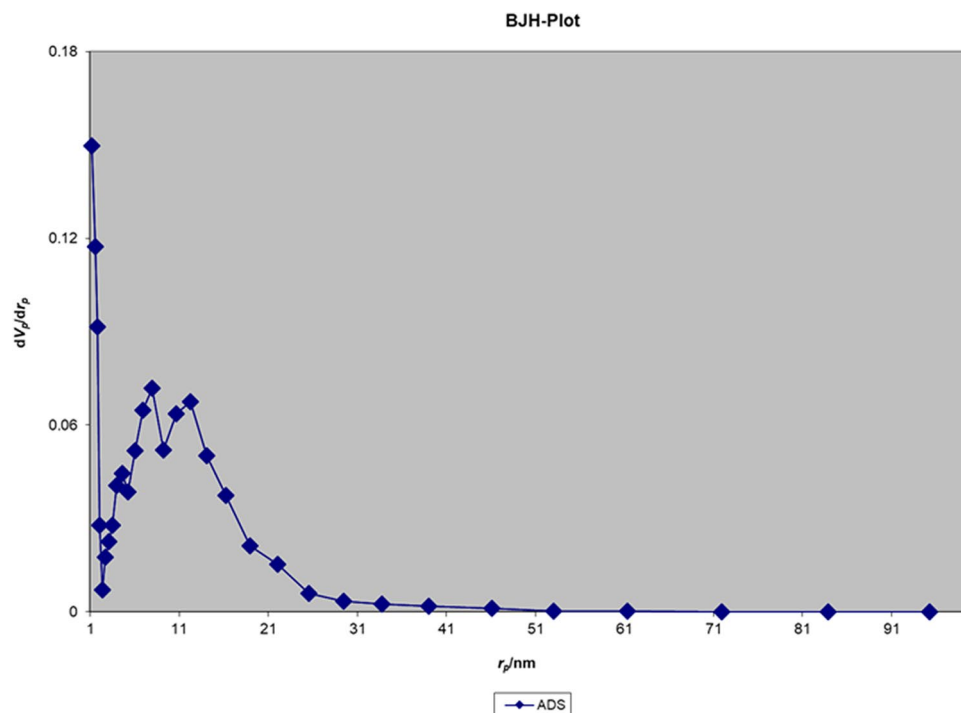
Figure 11. BJH pore size distribution isotherm of the Fe_3O_4@Void@m.SiO_2 nanomaterial before adsorption process.
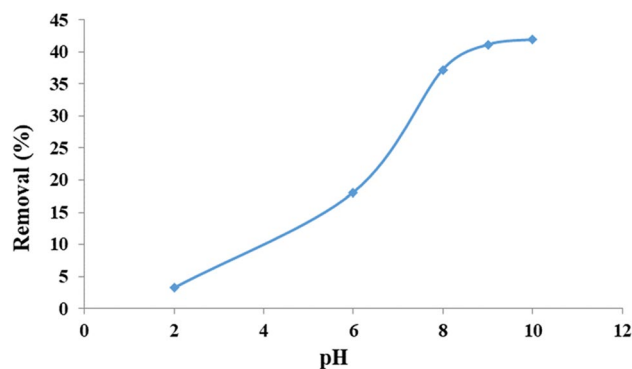

Figure 12. The effect of pH on MB adsorption.

and dye molecules. Accordingly, for 0.005 g of Fe_3O_4@Void@m.SiO_2 adsorbent, the optimum dye concentration was 5 ppm.

Effect of time. Figure 16 illustrates the time effect under optimum conditions. As seen, the rate of adsorption is high at first 3 min that can refer to adsorption by the outer surface of the shell. After that, this process is slowly increased with time. The latter adsorption can be happened on internal surface of the shell and also surface of the core. As shown, after 15 min the maximum adsorption is resulted.

Kinetics evaluation. To study the kinetics evaluation, the kinetic models of pseudo-first-order, second-order and Elovich were employed (Table 1). The pseudo-first-order model is as follows:

$$\log(q_e - q_t) = \frac{\log q_e - k_1 t}{2.303} \quad (3)$$

where q_t is the adsorbed dye at t time (mg/g); q_e is adsorbed dye at equilibrium (mg/g) and k_1 is the rate constant of adsorption (min^{-1}). The pseudo-second-order model is also as follows:
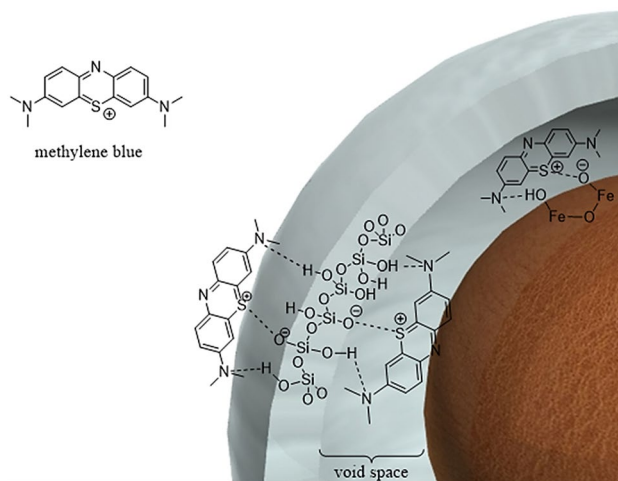
Figure 13. A suitable mechanism for MB adsorption using Fe_3O_4@Void@m.SiO$_2$.

Figure 14. The effect of Fe_3O_4@Void@m.SiO$_2$ amount on MB adsorption.

Figure 15. The effect of MB concentration using 0.005 g of adsorbent.

$$\frac{t}{q_t} = \frac{1}{k_2 q_e^2} + \frac{t}{q_e} \tag{4}$$

the q_e and k_2 were obtained via the plot of $\frac{t}{q_t}$ versus t (Fig. 17, Table 1). The Elovich equation is also as follows:

$$q_t = 1/\beta \ln(\alpha\beta) + 1/\beta \ln(t) \tag{5}$$

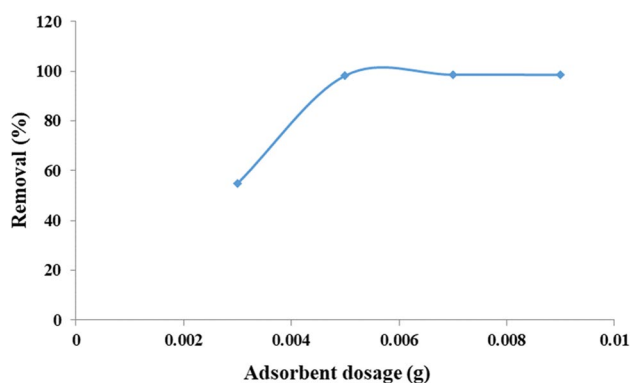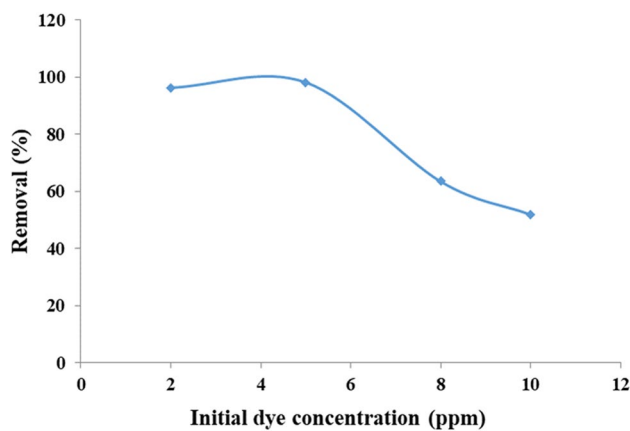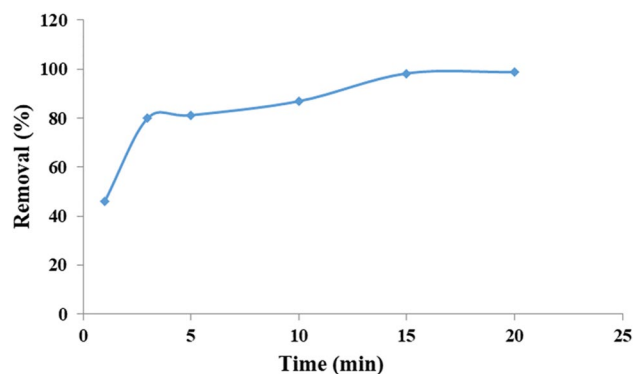**Figure 16.** Effect of time.

Model	Parameters	Adsorbent
		Fe$_3$O$_4$@Void@m.SiO$_2$
First-order kinetic	k$_1$	0.093
	qe (calc)	4.959
	R^2	0.808
Second-order kinetic	k$_2$	0.049
	q$_e$ (calc)	15.64
	R^2	0.997
Elovich	B	0.406
	A	59.943
	R^2	0.912

Table 1. Kinetic parameters for MB adsorption using Fe$_3$O$_4$@Void@m.SiO$_2$.
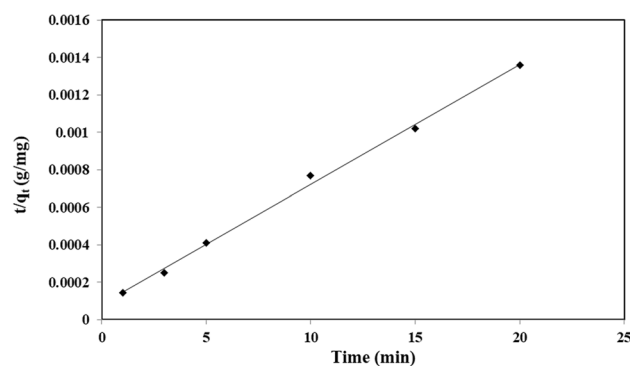
Figure 17. The pseudo-second-order plot of MB adsorption using Fe$_3$O$_4$@Void@m.SiO$_2$.

As shown in Table 1 and Fig. 17, the pseudo-second-order model with a linear regression correlation coefficient (R^2) value of 0.997 is completely applicable for the process.

Isotherm study. To determine the maximum capacity of sorption, the Langmuir, Freundlich and Temkin isotherm models were employed. The Langmuir model is as follows:

$$q_e = q_m \frac{K_L C_e}{1 + K_L C_e} \tag{6}$$

where q$_e$ is the equilibrium concentration of dye, q$_m$ is the maximum dye uptake and K$_L$ is Langmuir constant. These are determined by linearizing of Eq. (6) as shown in Eq. (7),

Isotherm	Parameters	Adsorbent
		Fe_3O_4@Void@m.SiO_2
Langmuir	Q_m(mg/g)	163.934
	K_a (L/mg)	0.095
	R^2	0.996
Freundlich	1/n	0.130
	K_F (L/mg)	349.945
	R^2	0.379
Tempkin	B_1	1.287
	K_T (L/mg)	34,166.468
	R^2	0.393

Table 2. Isotherm parameters and R^2 amounts obtained for the MB adsorption using Fe_3O_4@Void@m.SiO_2.
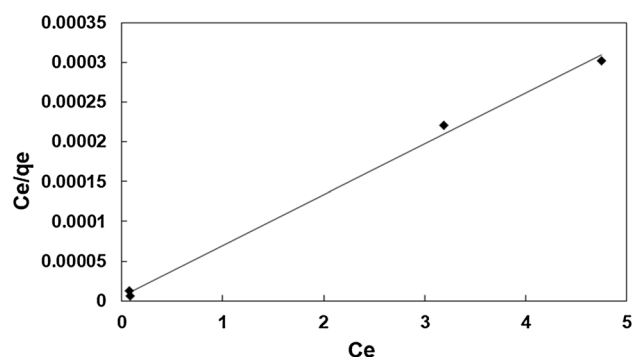

Figure 18. The Langmuir plot of MB adsorption by using Fe_3O_4@Void@m.SiO_2.

$$\frac{C_e}{q_e} = \frac{1}{K_L Q_m} + \frac{C_e}{Q_m} \tag{7}$$

The Freundlich model is also as follows:

$$q_e = K_F C_e^{1/n} \tag{8}$$

The linear form of above equation is Eq. (9) in which K_f and n are Freundlich constants

$$\log(q_e) = \log(K_F) + \frac{1}{n}\log(C_e) \tag{9}$$

The other isotherm model is Temkin with a linear form as follows:

$$q_e = B_T \ln K_T + B_T \ln C_e \tag{10}$$

As shown in Table 2 and Fig. 18, the Langmuir model with an $R^2 > 0.99$ is the best isotherm for the process.

Thermodynamic study. Thermodynamic parameters (ΔG^0, ΔH^0 and ΔS^0) were calculated by using following equations[51]:

$$K_c = \frac{q_e}{C_e} \tag{11}$$

$$\Delta G^0 = -RT \ln K_c \tag{12}$$

$$\Delta G^0 = \Delta H^0 - T\Delta S^0 \tag{13}$$

$$ln K_c = \frac{\Delta S^0}{R} - \frac{\Delta H^0}{RT} \tag{14}$$

These parameters are listed in Table 3. The plot of ln K_c versus 1/T is illustrated in Fig. 19. As shown, a satisfactory adsorption is resulted at RT and by increasing the temperature from 25 to 55 °C, a slight decrease in

Temperature (K)	ΔG^0 (kJ/mol)	ΔH^0 (kJ/mol)	ΔS^0 (J/mol K)	R^2
298	− 12.79			
308	− 11.65	− 43.94	− 104.65	0.999
318	− 10.65			
328	− 9.64			

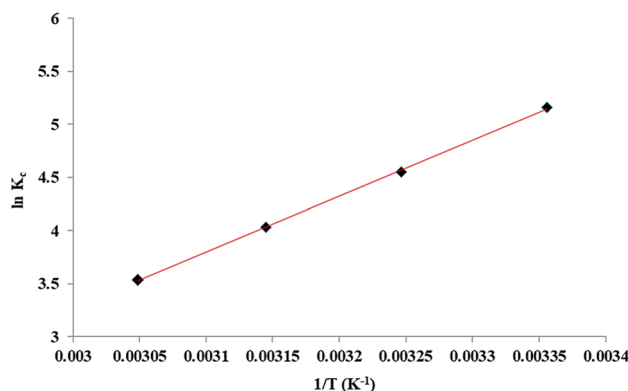**Table 3.** Thermodynamic parameters of MB adsorption using Fe_3O_4@Void@m.SiO_2.

Figure 19. The plot of ln K_c versus 1/T.

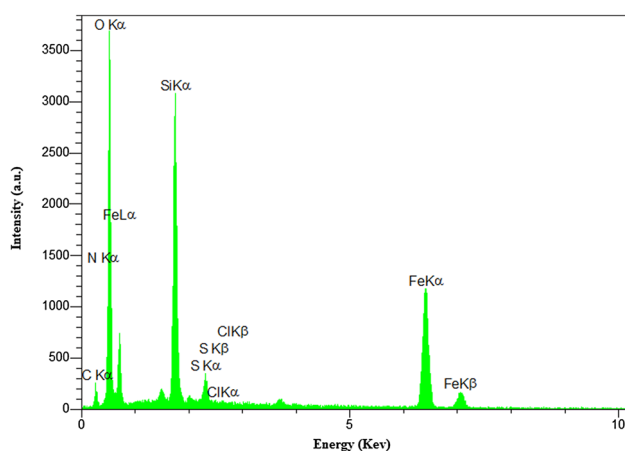**Figure 20.** The EDS analysis of Fe_3O_4@Void@m.SiO_2 nanomaterial after MB adsorption.

MB adsorption is observed indicating the process is exothermic. This was also confirmed by the negative $\Delta H°$. The negative amount of ΔG^0 confirms that the MB adsorption on Fe_3O_4@Void@m.SiO_2 is achievable and spontaneous. The negative $\Delta S°$ also suggests a decrease in randomness at solid/solution interface[52]. Moreover, the amounts of ΔH^0 and ΔG^0 successfully indicate that MB molecules are both physically and chemically adsorbed into/onto adsorbent material.

EDS spectrum. To investigate the successful adsorption of MB molecules into/onto Fe_3O_4@Void@m.SiO_2, the EDS analysis after adsorption process was performed (Fig. 20). As shown, the existence of new peaks of carbon, nitrogen, sulfur and chlorine in this spectrum confirms successful adsorption of MB molecules into/onto material.

Nitrogen adsorption–desorption and BJH pore size distribution isotherms. The nitrogen adsorption–desorption analysis of the Fe_3O_4@Void@m.SiO_2 nanomaterial after adsorption of MB was performed (Fig. 21). According to this analysis, the BET surface area and total pore volume of the Fe_3O_4@Void@m.SiO_2 nanomaterial after adsorption process were reduced to 142.32 m^2/g and 0.35 cm^3/g, respectively. The BJH pore size distribution isotherm after adsorption process also showed that the sizes of shell pores and void space between yolk and shell are 5.1 and 7.9, respectively (Fig. 22). Moreover, as shown in the Figs. 21 and 22, after the adsorption process the inten-
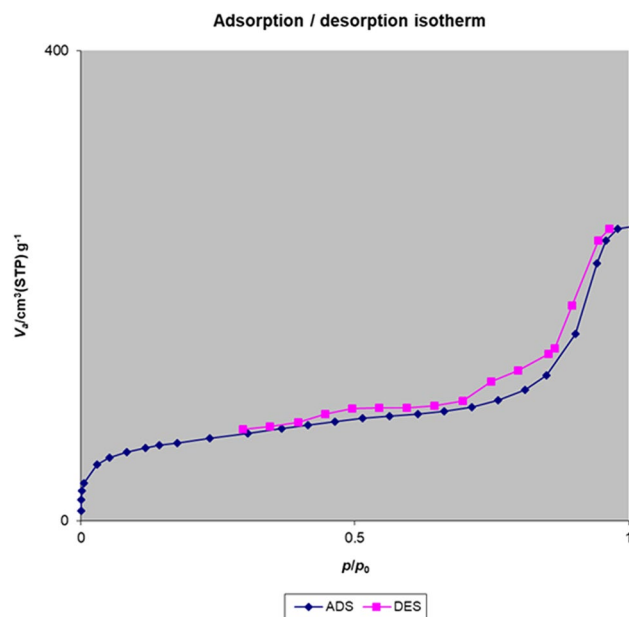
Figure 21. Nitrogen adsorption–desorption isotherm of the Fe_3O_4@Void@m.SiO_2 nanomaterial after adsorption process.
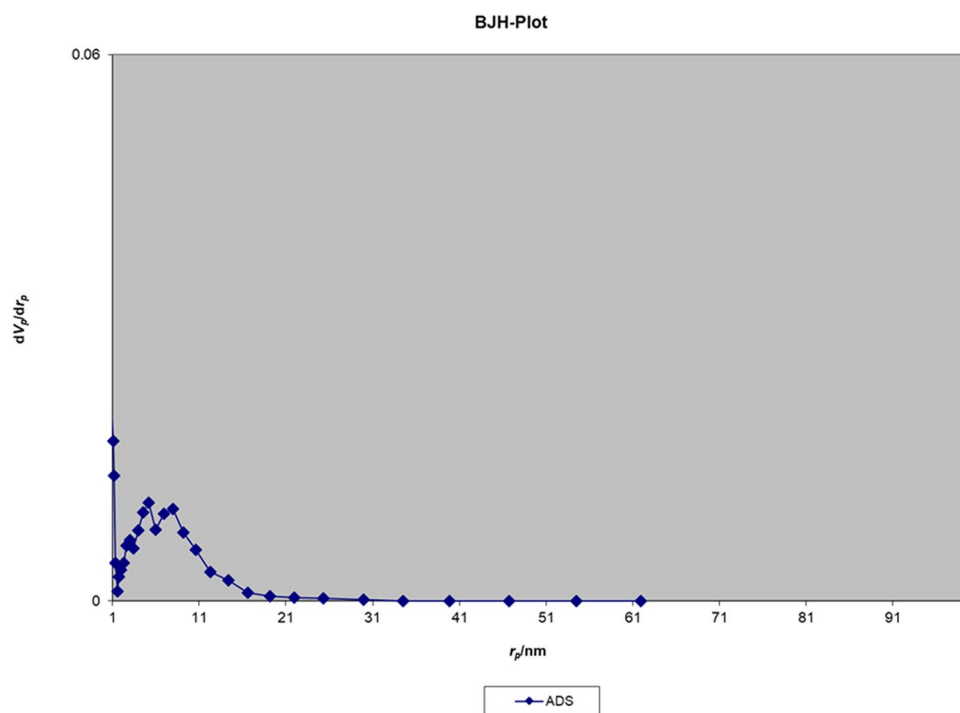
Figure 22. BJH pore size distribution isotherm of the Fe_3O_4@Void@m.SiO_2 nanomaterial after adsorption process.

sity of both adsorption–desorption and BJH isotherms are reduced in comparison to the fresh material. These observations confirm that both cavities and pores of the adsorbent are occupied by MB molecules.

Recoverability and reusability studies. In next step, the recoverability and reusability of the Fe_3O_4@Void@m.SiO_2 were investigated. To do this, the adsorbed MB molecules on Fe_3O_4@Void@m.SiO_2 were desorbed by acidic ethanol (pH 2). Then, the adsorbent was recovered and reused under the same conditions as the first run. As

Figure 23. Recoverability and reusability of Fe_3O_4@Void@m.SiO_2.

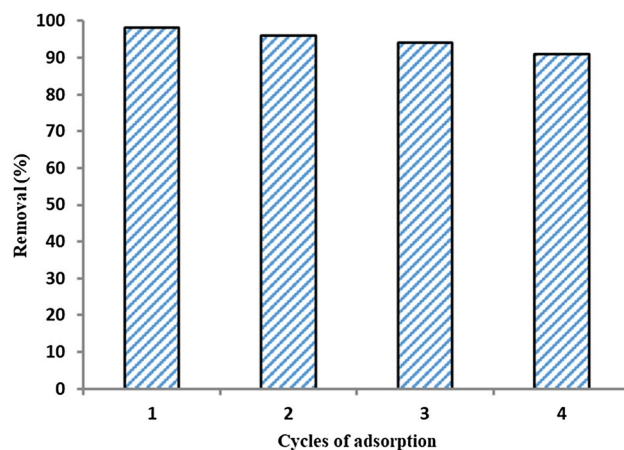| Entry	Adsorbent	Conditions	Adsorption efficiency (%)	Adsorption capacity (mg/g)	Recovery times	Ref
1	Graphene oxide/calcium alginate composite	3 h, 25 °C, 100 mL of 30–80 mg/L of MB solution, 0.05 g adsorbent	88.6–92.7	181.81	–	[53]
2	Activated carbon	1 h, 25 °C, 10 mL of 250–500–750 mg/L of MB solution, 0.05 g adsorbent	–	270.3	–	[54]
3	Polyaniline nanotubes base/silica composite	1 h, 25 °C, 100 mL of 3.1 mg/L of MB solution, 0.05 g adsorbent	–	0.61–5.38	–	[55]
4	Iron terephthalate (MOF-235)	1 h, 25 °C, 50 mL of 3.1 mg/L of MB solution, 0.05 g adsorbent	–	477	–	[56]
5	Nanocomposite of hydrolyzed poly-acrylamide grafted xanthan gum and incorporated nanosilica	20 min, 50 °C, 25 mL of 30 mg/L of MB solution, 0.03 g adsorbent	99.4	497.5	–	[57]
6	Fe_3O_4-graphene@mesoporous SiO_2 nanocomposites	15 min, 25 °C, 25 mL of 10 mg/L of MB solution, 0.01 g adsorbent	100	0.98–102.2	–	[58]
7	Yolk–shell tubular Fe_2O_3@magnesium silicate	15 h, 25 °C, 10 mL of 50 mg/L of MB solution, 0.01 g adsorbent	94	188	–	[59]
8	Fe_3O_4@SiO_2 composite (adsorption–photodegradation)	5 min, 25 °C, 10 mL of 10 mg/L of MB solution, 0.01 g adsorbent	99	33.12	5	[60]
9	Yolk shell magnetic Fe_3O_4@hierarchical hollow silica nanomaterials	1 h, 25 °C, 50 mL of 40 mg/L of MB solution, 0.05 g adsorbent	92	71.45	5	[18]
10	Fe_3O_4@Void@m.SiO_2 yolk–shell nanomaterial	15 min, 25 °C, 15 mL of 5 mg/L of MB solution, 0.005 g adsorbent	98.2	163.93	3	This work

Table 4. A comparison study between present adsorbent and previously reported adsorbents in the MB removal.

Fig. 23 shown, there is an insignificant decrease in adsorption ability of adsorbent after three cycles indicating the high stability and efficiency of designed Fe_3O_4@Void@m.SiO_2 for MB removal.

Comparison study. Next, the adsorption efficiency of our designed Fe_3O_4@Void@m.SiO_2 nanomaterial was compared with some reported adsorbents in MB adsorption (Table 4). As shown, in the most of previous studies the adsorbent is not recovered and also in some cases higher temperature than RT is needed for absorption. Moreover, the time required for absorption in most of former reports is high. These findings successfully confirm higher tendency and excellent capacity of the Fe_3O_4@Void@m.SiO_2 for adsorption of MB molecules in comparison to previous adsorbents.

Conclusion

In summary, a magnetic yolk–shell structured nanomaterial with mesoporous shell (Fe_3O_4@Void@m.SiO_2) was prepared, characterized and used as an effective adsorbent for the removal of MB dye from aqueous solution. The adsorption study showed that the designed material is so efficient with high removal capacity. Optimum conditions to achieve maximum removal of 98.2% for adsorption process were 0.005 g of adsorbent, pH 9 and 15 min for 15 mL of 5 mg/mL MB solution. The kinetic and isotherm studies of adsorption process were investigated and different models were evaluated for the equilibrium data. The results showed that the Langmuir isotherm model and pseudo-second-order kinetic are successfully fitted. The maximum adsorption capacity of the material was

163.93 mg/g. The comparison study illustrated that the present adsorbent is much more efficient than previously reported adsorbents in the removal of MB dye.

References

1. Kamata, K., Lu, Y. & Xia, Y. Synthesis and characterization of monodispersed core–shell spherical colloids with movable cores. *J. Am. Chem. Soc.* **125**, 2384–2385 (2003).
2. Kim, M., Sohn, K., Na, H. B. & Hyeon, T. Synthesis of nanorattles composed of gold nanoparticles encapsulated in mesoporous carbon and polymer shells. *Nano Lett.* **2**, 1383–1387 (2002).
3. Guo, C.-W., Cao, Y., Xie, S.-H., Dai, W.-L. & Fan, K.-N. Fabrication of mesoporous core-shell structured titania microspheres with hollow interiors. *Chem. Commun.*, 700–701 (2003).
4. Wang, W., Dahl, M. & Yin, Y. Hollow nanocrystals through the nanoscale Kirkendall effect. *Chem. Mater.* **25**, 1179–1189 (2013).
5. Fang, X. *et al.* Hollow mesoporous aluminosilica spheres with perpendicular pore channels as catalytic nanoreactors. *ACS Nano* **6**, 4434–4444 (2012).
6. Liu, J. *et al.* Yolk–shell hybrid materials with a periodic mesoporous organosilica shell: Ideal nanoreactors for selective alcohol oxidation. *Adv. Funct. Mater.* **22**, 591–599 (2012).
7. Cipolatti, E. P. *et al.* Nanomaterials for biocatalyst immobilization—State of the art and future trends. *RSC Adv.* **6**, 104675–104692 (2016).
8. Ni, W., Wang, Y. & Xu, R. Formation of Sn@ C yolk–shell nanospheres and core–sheath nanowires for highly reversible lithium storage. *Part. Part. Syst. Charact.* **30**, 873–880 (2013).
9. Song, H., Cui, H. & Wang, C. Abnormal cyclicity in Ni@ graphene core–shell and yolk–shell nanostructures for lithium ion battery anodes. *ACS Appl. Mater. Interfaces* **6**, 13765–13769 (2014).
10. Li, X. *et al.* Design of Au@ ZnO yolk–shell nanospheres with enhanced gas sensing properties. *ACS Appl. Mater. Interfaces* **6**, 18661–18667 (2014).
11. Rai, P. *et al.* Design of highly sensitive and selective Au@ NiO yolk–shell nanoreactors for gas sensor applications. *Nanoscale* **6**, 8292–8299 (2014).
12. Wang, S., Zhang, M. & Zhang, W. Yolk– shell catalyst of single Au nanoparticle encapsulated within hollow mesoporous silica microspheres. *ACS Catal.* **1**, 207–211 (2011).
13. Zhang, J., Li, B. & Yang, W. Synthesis and photocatalytic performance of novel hierarchical hollow silica sphere supported TiO2 nanoparticles. *Mater. Lett.* **117**, 252–255 (2014).
14. Norouzi, M. & Elhamifar, D. Magnetic yolk–shell structured methylene and propylamine based mesoporous organosilica nano-composite: A highly recoverable and durable nanocatalyst with improved efficiency. *Colloids Surf. A Physicochem. Eng. Asp.* **615**, 126226 (2021).
15. Mirbagheri, R., Elhamifar, D. & Hajati, S. Ru-containing magnetic yolk–shell structured nanocomposite: A powerful, recoverable and highly durable nanocatalyst. *RSC Adv.* **11**, 10243–10252 (2021).
16. Shaker, M. & Elhamifar, D. Cu-containing magnetic yolk–shell structured ionic liquid-based organosilica nanocomposite: A powerful catalyst with improved activity. *Compos. Commun.* **24**, 100608 (2021).
17. Fan, H., Lei, Z., Pan, J. H. & Zhao, X. Sol–gel synthesis, microstructure and adsorption properties of hollow silica spheres. *Mater. Lett.* **65**, 1811–1814 (2011).
18. Zhang, J., Li, B., Yang, W. & Liu, J. Synthesis of magnetic Fe3O4@ hierarchical hollow silica nanospheres for efficient removal of methylene blue from aqueous solutions. *Ind. Eng. Chem. Res.* **53**, 10629–10636 (2014).
19. Liu, J. *et al.* Uniform yolk–shell Sn 4 P 3@ C nanospheres as high-capacity and cycle-stable anode materials for sodium-ion batteries. *Energy Environ. Sci.* **8**, 3531–3538 (2015).
20. Cho, J. S. & Kang, Y. C. Nanofibers comprising yolk–shell Sn@ void@ SnO/SnO2 and hollow SnO/SnO2 and SnO2 nanospheres via the Kirkendall diffusion effect and their electrochemical properties. *Small* **11**, 4673–4681 (2015).
21. Li, S. *et al.* High-rate aluminium yolk–shell nanoparticle anode for Li-ion battery with long cycle life and ultrahigh capacity. *Nat. Commun.* **6**, 1–7 (2015).
22. Evangelista, V. *et al.* Highly active Au-CeO2@ ZrO2 yolk–shell nanoreactors for the reduction of 4-nitrophenol to 4-aminophenol. *Appl. Catal. B* **166**, 518–528 (2015).
23. Du, X. & He, J. Spherical silica micro/nanomaterials with hierarchical structures: Synthesis and applications. *Nanoscale* **3**, 3984–4002 (2011).
24. Li, Z. *et al.* Measurement of uptake and release capacities of mesoporous silica nanoparticles enabled by nanovalve gates. *J. Phys. Chem. C* **115**, 19496–19506 (2011).
25. Purbia, R. & Paria, S. Yolk/shell nanoparticles: Classifications, synthesis, properties, and applications. *Nanoscale* **7**, 19789–19873 (2015).
26. Wang, Q., Liu, Y. & Yan, H. Mechanism of a self-templating synthesis of monodispersed hollow silica nanospheres with tunable size and shell thickness. *Chem. Commun.*, 2339–2341 (2007).
27. Zoldesi, C. I., van Walree, C. A. & Imhof, A. Deformable hollow hybrid silica/siloxane colloids by emulsion templating. *Langmuir* **22**, 4343–4352 (2006).
28. Park, J.-I. & Cheon, J. Synthesis of "solid solution" and "core-shell" type cobalt–platinum magnetic nanoparticles via transmetalation reactions. *J. Am. Chem. Soc.* **123**, 5743–5746 (2001).
29. Piao, Y. *et al.* Wrap–bake–peel process for nanostructural transformation from β-FeOOH nanorods to biocompatible iron oxide nanocapsules. *Nat. Mater.* **7**, 242–247 (2008).
30. Lee, J.-H. *et al.* Artificially engineered magnetic nanoparticles for ultra-sensitive molecular imaging. *Nat. Med.* **13**, 95–99 (2007).
31. Wu, X. *et al.* Immunofluorescent labeling of cancer marker Her2 and other cellular targets with semiconductor quantum dots. *Nat. Biotechnol.* **21**, 41–46 (2003).
32. Dubertret, B. *et al.* In vivo imaging of quantum dots encapsulated in phospholipid micelles. *Science* **298**, 1759–1762 (2002).
33. Elhamifar, D., Mofatehnia, P. & Faal, M. Magnetic nanoparticles supported Schiff-base/copper complex: An efficient nanocatalyst for preparation of biologically active 3, 4-dihydropyrimidinones. *J. Colloid Interface Sci.* **504**, 268–275 (2017).
34. Elhamifar, D., Ramazani, Z., Norouzi, M. & Mirbagheri, R. Magnetic iron oxide/phenylsulfonic acid: A novel, efficient and recoverable nanocatalyst for green synthesis of tetrahydrobenzo [b] pyrans under ultrasonic conditions. *J. Colloid Interface Sci.* **511**, 392–401 (2018).
35. Mousavi, F., Elhamifar, D. & Kargar, S. Copper/IL-containing magnetic nanoporous MCM-41: A powerful and highly stable nanocatalyst. *Surf. Interfaces* **25**, 101225 (2021).
36. Dutta, K., Mukhopadhyay, S., Bhattacharjee, S. & Chaudhuri, B. Chemical oxidation of methylene blue using a Fenton-like reaction. *J. Hazard. Mater.* **84**, 57–71 (2001).

37. Lachheb, H. *et al.* Photocatalytic degradation of various types of dyes (Alizarin S, Crocein Orange G, Methyl Red, Congo Red, Methylene Blue) in water by UV-irradiated titania. *Appl. Catal. B* **39**, 75–90 (2002).
38. Oliveira, L. C., Petkowicz, D. I., Smaniotto, A. & Pergher, S. B. Magnetic zeolites: A new adsorbent for removal of metallic contaminants from water. *Water Res.* **38**, 3699–3704 (2004).
39. Peng, X., Luan, Z., Di, Z., Zhang, Z. & Zhu, C. Carbon nanotubes-iron oxides magnetic composites as adsorbent for removal of Pb (II) and Cu (II) from water. *Carbon* **43**, 880–883 (2005).
40. Fei, P., Zhong, M., Lei, Z. & Su, B. One-pot solvothermal synthesized enhanced magnetic zinc ferrite–reduced graphene oxide composite material as adsorbent for methylene blue removal. *Mater. Lett.* **108**, 72–74 (2013).
41. Jiang, T., Liang, Y.-D., He, Y.-J. & Wang, Q. Activated carbon/NiFe$_2$O$_4$ magnetic composite: A magnetic adsorbent for the adsorption of methyl orange. *J. Environ. Chem. Eng.* **3**, 1740–1751 (2015).
42. Mirbagheri, R., Elhamifar, D. & Norouzi, M. Propylamine-containing magnetic ethyl-based organosilica with a core–shell structure: An efficient and highly stable nanocatalyst. *New J. Chem.* **42**, 10741–10750 (2018).
43. Dai, J. *et al.* Yolk–shell Fe$_3$O$_4$@ SiO$_2$@PMO: Amphiphilic magnetic nanocomposites as an adsorbent and a catalyst with high efficiency and recyclability. *Green Chem.* **19**, 1336–1344 (2017).
44. Wang, L. *et al.* Adsorption of Pb (II) on activated carbon prepared from *Polygonum orientale* Linn.: Kinetics, isotherms, pH, and ionic strength studies. *Bioresour. Technol.* **101**, 5808–5814 (2010).
45. Sousa, H. R. *et al.* Evaluation of methylene blue removal by plasma activated palygorskites. *J. Mater. Res. Technol.* **8**, 5432–5442 (2019).
46. Şahin, Ö., Kaya, M. & Saka, C. Plasma-surface modification on bentonite clay to improve the performance of adsorption of methylene blue. *Appl. Clay Sci.* **116**, 46–53 (2015).
47. Adeyemo, A. A., Adeoye, I. O. & Bello, O. S. Adsorption of dyes using different types of clay: A review. *Appl. Water Sci.* **7**, 543–568 (2017).
48. El Qada, E. N., Allen, S. J. & Walker, G. M. Adsorption of basic dyes from aqueous solution onto activated carbons. *Chem. Eng. J.* **135**, 174–184 (2008).
49. Chandrasekhar, S. & Pramada, P. Rice husk ash as an adsorbent for methylene blue—Effect of ashing temperature. *Adsorption* **12**, 27–43 (2006).
50. Hamdaoui, O. Batch study of liquid-phase adsorption of methylene blue using cedar sawdust and crushed brick. *J. Hazard. Mater.* **135**, 264–273 (2006).
51. You, L., Wu, Z., Kim, T. & Lee, K. Kinetics and thermodynamics of bromophenol blue adsorption by a mesoporous hybrid gel derived from tetraethoxysilane and bis (trimethoxysilyl) hexane. *J. Colloid Interface Sci.* **300**, 526–535 (2006).
52. Alkan, M., Demirbaş, Ö. & Doğan, M. Adsorption kinetics and thermodynamics of an anionic dye onto sepiolite. *Microporous Mesoporous Mater.* **101**, 388–396 (2007).
53. Li, Y. *et al.* Methylene blue adsorption on graphene oxide/calcium alginate composites. *Carbohydr. Polym.* **95**, 501–507 (2013).
54. Dural, M. U., Cavas, L., Papageorgiou, S. K. & Katsaros, F. K. Methylene blue adsorption on activated carbon prepared from *Posidonia oceanica* (L.) dead leaves: Kinetics and equilibrium studies. *Chem. Eng. J.* **168**, 77–85 (2011).
55. Ayad, M. M., El-Nasr, A. A. & Stejskal, J. Kinetics and isotherm studies of methylene blue adsorption onto polyaniline nanotubes base/silica composite. *J. Ind. Eng. Chem.* **18**, 1964–1969 (2012).
56. Haque, E., Jun, J. W. & Jhung, S. H. Adsorptive removal of methyl orange and methylene blue from aqueous solution with a metal–organic framework material, iron terephthalate (MOF-235). *J. Hazard. Mater.* **185**, 507–511 (2011).
57. Ghorai, S. *et al.* Enhanced removal of methylene blue and methyl violet dyes from aqueous solution using a nanocomposite of hydrolyzed polyacrylamide grafted xanthan gum and incorporated nanosilica. *ACS Appl. Mater. Interfaces* **6**, 4766–4777 (2014).
58. Wu, X.-L., Shi, Y., Zhong, S., Lin, H. & Chen, J.-R. Facile synthesis of Fe$_3$O$_4$-graphene@ mesoporous SiO$_2$ nanocomposites for efficient removal of Methylene Blue. *Appl. Surf. Sci.* **378**, 80–86 (2016).
59. Zheng, J. *et al.* Synthesis of yolk–shell magnetic magnesium silicate with tunable yolk morphology for removal of methylene blue in water. *J. Alloys Compd.* **596**, 5–9 (2014).
60. Tan, X., Lu, L., Wang, L. & Zhang, J. Facile synthesis of bimodal mesoporous Fe$_3$O$_4$@SiO$_2$ composite for efficient removal of methylene blue. *Eur. J. Inorg. Chem.* **2015**, 2928–2933 (2015).

Acknowledgements

Author contributions

R.M.: Investigation, Writing—Original Draft, Resources, Formal analysis.D.E.: Conceptualization, Writing—Review and Editing, Supervision, Visualization.M.S.: Resources, Formal analysis.

Competing interests

The authors declare no competing interests.

Additional information

Correspondence and requests for materials should be addressed to D.E.

Reprints and permissions information is available at www.nature.com/reprints.

Publisher's note Springer Nature remains neutral with regard to jurisdictional claims in published maps and institutional affiliations.